Biomaterials Advances 163 (2024) 213968

Contents lists available at ScienceDirect

Biomaterials Advances

journal homepage: www.journals.elsevier.com/materials-science-and-engineering-c

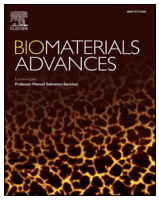

Regulation of osteogenesis and angiogenesis by cobalt, manganese and strontium doped apatitic materials for functional bone tissue regeneration

Francesca Silingardi [a], Francesca Salamanna [b], Montserrat Español [c], Melania Maglio [b], Maria Sartori [b], Gianluca Giavaresi [b], Adriana Bigi [a], Maria-Pau Ginebra [c], Elisa Boanini [a,*]

[a] Department of Chemistry "Giacomo Ciamician", Alma Mater Studiorum - University of Bologna, 40126 Bologna, Italy
[b] Surgical Sciences and Technologies, IRCCS Istituto Ortopedico Rizzoli, 40136 Bologna, Italy
[c] Biomaterials, Biomechanics and Tissue Engineering Group, Department of Materials Science and Engineering, Universitat Politècnica de Catalunya (UPC), Barcelona 08019, Spain

ARTICLE INFO

Keywords:
Ionic substitution
Brushite
Hydroxyapatite
Human mesenchymal stem cell
Osteoclast

ABSTRACT

Strontium, cobalt, and manganese ions are present in the composition of bone and useful for bone metabolism, even when combined with calcium phosphate in the composition of biomaterials. Herein we explored the possibility to include these ions in the composition of apatitic materials prepared through the cementitious reaction between ion-substituted calcium phosphate dibasic dihydrate, $CaHPO_4{\cdot}2H_2O$ (DCPD) and tetracalcium phosphate, $Ca_4(PO_4)_2O$ (TTCP). The results of the chemical, structural, morphological and mechanical characterization indicate that cobalt and manganese exhibit a greater delaying effect than strontium (about 15 at.%) on the cementitious reaction, even though they are present in smaller amounts within the materials (about 0.8 and 4.5 at.%, respectively). Furthermore, the presence of the foreign ions in the apatitic materials leads to a slight reduction of porosity and to enhancement of compressive strength. The results of biological tests show that the presence of strontium and manganese, as well as calcium, in the apatitic materials cultured in direct contact with human mesenchymal stem cells (hMSCs) stimulates their viability and activity. In contrast, the apatitic material containing cobalt exhibits a lower metabolic activity. All the materials have a positive effect on the expression of Vascular Endothelial Growth Factor (VEGF) and Von Willebrand Factor (vWF). Moreover, the apatitic material containing strontium induces the most significant reduction in the differentiation of preosteoclasts into osteoclasts, demonstrating not only osteogenic and angiogenic properties, but also ability to regulate bone resorption.

1. Introduction

Deposition of the inorganic phase in bone tissue occurs in an environment rich of ions, which display specific biological roles [1,2]. Partial substitution of calcium with biological relevant ions is an interesting method to enrich biocompatible and bioactive calcium orthophosphates (CaPs) with specific properties [3,4]. CaPs are indeed widely investigated as components of biomaterials with potential applications for the substitution and/or repair of the hard tissues of vertebrates. In this field, a great deal of attention is addressed to calcium phosphate cements, CPCs [5,6]. The composition of CPCs involves one or more calcium phosphates, which, once mixed with a liquid phase, yield a workable paste that hardens with time. The final phase is a calcium phosphate more thermodynamically stable than the starting materials, usually brushite, $CaHPO_4{\cdot}2H_2O$ (DCPD) or hydroxyapatite, either stoichiometric, $Ca_{10}(PO_4)_6(OH)_2$ (HA) or calcium-deficient (CDHA) [6]. Since the first development of CPCs by Brown and Chow [7], several different formulations have been proposed [5,6,8–10]. Moreover, CPCs compositions have been enriched with a variety of additives, including biological relevant anions and cations, which have been usually added as other calcium salts and as compounds of cations different from calcium [11–15].

Herein, we investigated the role of cobalt, manganese and strontium, which are present in the composition of bone [16], on the properties of apatitic materials obtained through a cementitious reaction between calcium phosphate dibasic dihydrate, $CaHPO_4{\cdot}2H_2O$ (DCPD) and tetracalcium phosphate, $Ca_4(PO_4)_2O$ (TTCP).

Hard tissues of vertebrates contain up to 1 ppm of Co^{2+} [1], which is also present in vitamin B12 [17]. Co^{2+} has been reported to promote angiogenesis and osteogenesis [18,19]. Cobalt-doped mesoporous

* Corresponding author.
E-mail address: elisa.boanini@unibo.it (E. Boanini).

https://doi.org/10.1016/j.bioadv.2024.213968
Received 29 November 2023; Received in revised form 13 May 2024; Accepted 22 July 2024
Available online 23 July 2024

hydroxyapatite enhanced the expression of vascular endothelial growth factor (VEGF) and hypoxia-inducible factor 1α (HIF-1α) in the MG-63 cells [20]. Moreover, the presence of small amount of Co^{2+} ions (up to 1 %) in brushitic cements has been reported to reduce hypoxia induced gene expression in osteosarcoma cells [17], whereas greater amounts were reported to reduce the number of attached osteoclast while enhancing their activity [21].

Manganese displays an essential role in the formation of cartilage and bone [22]; moreover, its association with calcium phosphates was found to increase osteoblast adhesion, proliferation and activity [23–25]. Wu et al. recently showed that relatively low contents of Mn^{2+} in the composition of apatitic cements can improve osteoblast viability, proliferation, as well as the levels of expression of several genes [22]. Furthermore, it was shown that the addition of divalent Mn^{2+} ions to mesoporous hydroxyapatite influences the activation of integrin with greater affinity and so osteoblast adhesion might occur *via* signaling cascades [26,27]. Thus, manganese incorporation has proved to be reliable in the calcination process, bio-mineralization, bone formation and reduces bone resorption.

The presence of strontium in bone is significantly higher than that of cobalt and manganese, and is particularly high in new bone, which is characterized by high metabolic turnover [1]. The great deal of research carried out on this ion indicates that it displays different effects on bone cells: it promotes adhesion, proliferation and differentiation of osteoblast, whereas it inhibits osteoclastogenesis and osteoclast activity, both *in vitro* and *in vivo* [28,29], also when it is associated to CaPs [30–37]. The dual impact of strontium on bone cells suggests that it enhances bone growth while reducing bone resorption, making strontium a valuable tool in the fight against osteoporosis [28,29,38,39].

Strontium, cobalt and manganese have been previously added to the composition of calcium phosphate bone cements with the aim to enrich the cements with the biological properties of these ions, as well as to modulate the physico-chemical properties of the cements. Both cobalt and manganese have been usually introduced in relatively small amounts in one of the components of the cement powder, namely β-tricalcium phosphate (β-TCP) [17,21,22,40]. The addition of strontium has been carried out using also different phosphates, such as octacalcium phosphate (OCP) and α-tricalcium phosphate (α-TCP), and different salts, including strontium ranelate, strontium carbonate and strontium chloride [30,31,34,36,41–43].

In this work, we utilized ion-substituted DCPD to introduce cobalt, manganese and strontium in the composition of apatitic materials obtained through a cementitious reaction. We have previously investigated the possible substitution of these ions to calcium in the structure of brushite and verified that the maximum substitution amounts are about 1, 7 and 30 at.% for Co^{2+}, Mn^{2+} and Sr^{2+} respectively [44]. Herein we report the results of a study on the influence of these ions on the hardening, structure, porosity and mechanical properties of the apatitic materials, as well as on the viability and differentiation of human mesenchymal stem cells (hMSC).

2. Materials and methods

2.1. Syntheses of crystalline powders

DCPD and TTCP were the two reactants used for the preparation of the materials. DCPD was used pure or substituted with bivalent cations, namely cobalt, manganese and strontium.

DCPD was obtained by direct precipitation in solution: 750 ml of a phosphate solution containing Na_2HPO_4 (0.033 M) and NaH_2PO_4 (0.033 M) was heated at 37 °C, and the pH was adjusted to 5 with glacial CH_3COOH; a calcium solution (250 ml) containing $Ca(CH_3COO)_2{\cdot}H_2O$ (0.2 M) was added dropwise (2 ml/min) to the phosphate solution under stirring (120 rpm). The solution was then stirred for 10 min, filtered, washed with distilled water, and dried overnight at 37 °C. All reagents were of analytical grade (Sigma Aldrich, USA). Substituted DCPD was obtained following the same procedure and partially substituting Ca $(CH_3COO)_2{\cdot}H_2O$ with $Co(CH_3COO)_2{\cdot}4H_2O$, $Mn(CH_3COO)_2{\cdot}4H_2O$ and Sr $(CH_3COO)_2{\cdot}1/2H_2O$. The concentrations in solution for the substituting ions were 25 at.% for cobalt, 20 at.% for manganese and 60 at.% for strontium, calculated as $[M^{2+}/(Ca^{2+}+M^{2+})]{\cdot}100$ and correspond to the highest possible substitution ratio in DCPD for the selected ions [44]. The total cation concentration was always kept at 0.2 M. The solid products are labelled DCPD-Co, DCPD-Mn and DCPD-Sr, respectively.

TTCP was obtained through a solid-state reaction. Dicalcium phosphate anhydrous ($CaHPO_4$) and calcium carbonate ($CaCO_3$) were combined in a 1:1 M ratio, mixed for 15 min with a Whip Mix and then placed in a platinum crucible. The mixture was heated to 1500 °C through a six-step ramp (0–300 °C 2.5 °C/min; 300 °C for 120 min; 300–1100 °C 2.5 °C/min; 1100 °C for 120 °C; 1100–1500 °C 2.5 °C/min; 1500 °C for 300 min) followed by quenching in air. The obtained TTCP power was then milled at 450 rpm for 2 min with 10BB (Big balls of agate).

2.2. Materials preparation

Pastes were prepared mixing DCPD (pure and substituted) and TTCP in molar ratio 1:1, liquid phase (H_3PO_4 20 mM) was added in order to obtain a L/P ratio of 0.3 ml/g, and the mixture was mixed for 30s at 2500 rpm with a Speedmixer DAC 150.1 FV-K. Then, the paste was used to fill disk moulds (6 mm diameter) and allowed to harden at 37 °C in 100 % relative humidity (RH).

The reaction that led to formation of an apatitic phase can be written as [45]:

$$Ca_4(PO_4)_2O + CaHPO_4\ 2H_2O \rightarrow Ca_5(PO_4)_3OH + 2H_2O.$$

Hardening was stopped after different times (up to 7 days) through 1 h immersion in EtOH; then samples were allowed to dry in air overnight.

The materials obtained using DCPD and DCPD with a partial substitution of calcium with Co, Mn and Sr ions were labelled c-Ca, c-Co, c-Mn and c-Sr, respectively.

2.2.1. Characterization

X-ray diffraction (XRD) patterns were collected in the 2θ range of 3–60° with a step of 0.1° and time/step of 100 s (PANalytical X'Pert PRO diffractometer in the Bragg−Brentano geometry equipped with a X'Celerator detector). The HighScore Plus program was used for phase identification, quantitative determination of the different phases, and structural refinements, using the Rietveld method (HighScore Plus software version 4.9, year 2020, by PANalytical B.V., Almelo, The Netherlands).

The metal content of both the starting powders and the final materials was determined through Inductively Coupled Plasma - Mass Spectrometry (ICP-MS, 7800 ICP-MS, Agilent). For the starting powders (DCPD and substituted DCPD), about 10 mg were digested in 1 ml of HNO_3 20 % overnight; for final materials, 45 mg were digested in 1 ml of HNO_3 20 % overnight. After digestion, 9 ml of millliQ water were added, the solutions were filtered with a membrane filter (0.22 μm) and then analyzed. Results were performed in quintuple.

To determine the ion release (Ca, Co, Mn, and Sr) a round-shaped disk of material (6 mm diameter, around 10 mg) was placed in 1 ml of solution (Tris(hydroxymethyl)aminomethane - TRIS 0.1 M or Saline 0.9 % NaCl). The supernatant was changed at each time point ($t = 5$ h, 1, 3, 5, 7 and 13 days). Investigation in saline was carried out on materials hardened for 7 days; whereas investigation in TRIS was carried out on materials hardened for 8 h and 7 days. All release tests were done in triplicate, results represent the mean value of three different determinations. The ion release was determined through Inductively Coupled Plasma - Mass Spectrometry (ICP-MS, 7800 ICP-MS, Agilent). Samples were prepared adding 0.3 ml of the supernatant into 2.7 ml of HNO_3 2 %. The solutions were filtered with a membrane filter (0.22 μm) and then analyzed.

Materials surfaces and cross sections were investigated by a JEOL

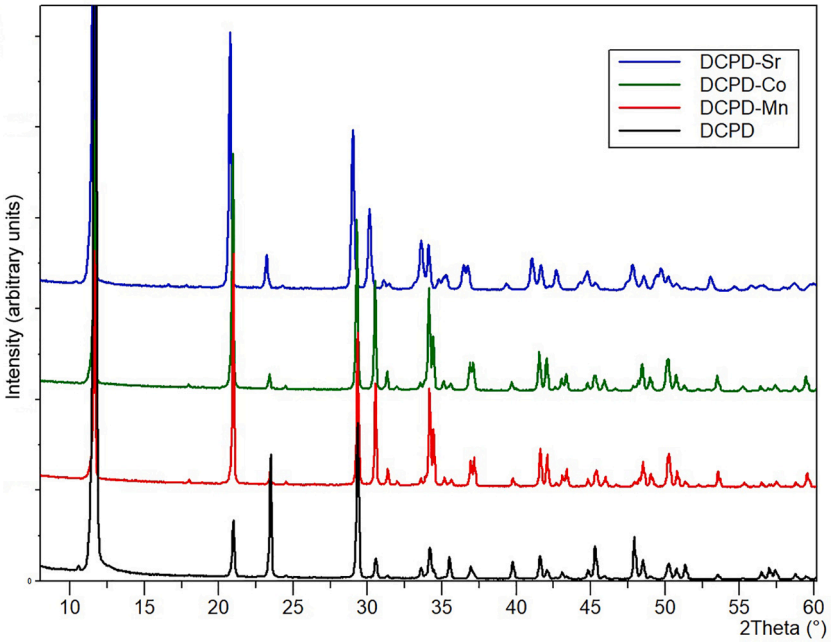

Fig. 1. XRD patterns of DCPD and ion-substituted DCPD powders.

JSM-7001F Schottky Emission Scanning electron microscope operating at 2 kV. The samples were placed on a carbon tape on aluminum sample-holders and then carbon-evaporated to minimise charging effects (K950X Turbo Evaporator, Emitech).

Mercury intrusion porosimetry (MIP, Autopore IV 9500 Micromeritics) was carried out to examine the porosity content (open porosity). Data were collected on cylinders with a height of 12 mm and a diameter of 6 mm. All samples were degassed under vacuum (10 mmHg) for 24 h, at 100 °C, prior to the measurement.

The mechanical behaviour was investigated by conducting a compression test in a universal testing machine (Bionix 858, MTS Systems) equipped with a 2.5kN load cell. Data were collected on wet (overnight submersion in 0.9 % NaCl solution) cylindrical specimen (12 mm height and 6 mm diameter) with a cross-head speed of 1 mm/min. Results are the average over 12 measurements.

Two samples of each type (c-Ca, c-Mn, c-Co, c-Sr) were scanned with a high resolution μCT system (Skyscan 1172, Bruker-MicroCT, Belgium) at a nominal resolution of 5 μm (2096 × 4000 pixels), applying an X-ray tube voltage of 70 kV and a 0.5 mm thick aluminum filter. The scan orbit was 180° with a rotation step of 0.3°. Reconstruction was carried out using the SkyScan TM NRecon software (version 1.7.4.6, Bruker). In addition to the specific alignment relative to each single scan, Gaussian smoothing, ring artifact reduction and beam hardening correction were applied during the reconstruction process. The quantitative morphometric analysis on μCT datasets was carried out using CTAn software (version 1.20.8.0, Bruker) defining for each sample a cylindrical Volume of interest (VOI) of 4.5 mm in diameter and 2 mm in height. The total porosity P.tot (%), defined as the ratio between the volume of the pores detected in the scaffolds and the total volume (VOI) was calculated for each sample.

2.3. Biological tests

For biological evaluation, round-shaped disks (diameter 6 mm, height about 2 mm) were sterilized using gamma rays (Cobalt-60) at a dose of 25 kGy.

2.3.1. In vitro culture model

Human mesenchymal stem cells (hMSC, Poietics™ Stem Cells, Lonza Walkersville, USA, batch 21TL116647, passage 2) derived from bone marrow were cultured in Mesenchymal Stem Cell Basal Medium (MSCBM, Poietics™ Lonza Walkersville, USA supplemented with 10 % fetal bovine serum (FBS, Lonza, Verviers, Belgium), 100 U/ml penicillin, 100 μg/ml streptomycin (Gibco, Life Technologies, Carlsbad, CA) and 5 μg/ml plasmocin (Invivogen, San Diego, CA), and incubated at 37 °C in a humidified 95%air/5%CO_2 atmosphere (standard condition). At 80 % confluence, hMSC were counted and seeded on the top of materials, c-Mn, c-Co and c-Sr, at 5 × 10^4 cells/material for 3, 7 and 14 days. The cells (5 × 10^4) were resuspended in a small volume of medium equal to 15 μl, to allow for complete attachment of the cells onto the material, preventing their dispersion.

Two control groups with only hMSC (Ctr-hMSC) and with c-Ca material with hMSC were prepared respectively to verify regular cell proliferation and differentiation, regardless of material presence and regular cell proliferation and differentiation on a control material without ions.

2.3.2. Cell viability.

Alamar blue dye (Serotec, Oxford, UK) was added to hMSCs (1:10 *v/v*) cultured in direct contact with the materials (experimental and control) and in Ctr-hMSC (hMSC alone), and incubated for 4 h at 37 °C. This non-toxic reagent allows evaluation of the cell activity on the same culture at different endpoints by the chemical reduction of its main component (resazurin) into resorufin in the mitochondria of living cells. The fluorescent product was quantified at 530ex–590em nm wavelengths using a microplate reader (VICTOR X2030, Perkin Elmer, Milano, Italy) and expressed as relative fluorescence units (RFU).

2.3.3. Quantitative polymerase chain reaction (qPCR)

Total RNA was extracted from hMSCs seeded on c-Ca, c-Mn, c-Co, c-Sr materials at 3, 7 and 14 days of culture, as well as from Ctr-hMSC (cells without materials), using Trizol® reagent (AMBION by Life Technologies, Carlsbad, CA, USA) and Chloroform (Sigma Aldrich) until harvesting the aqueous phase. The procedure was continued by using the commercial PureLinkTM RNeasy Mini Kit (AMBION), quantified by NANODROP spectrophotometer (NANODROP 2720, Thermal Cycler, Applied Biosystem) and reverse transcribed with SuperScriptVILO cDNA Synthesis Kit (Life Technologies), following the manufacturer's

Table 1
Cell parameters of pure and substituted DCPD calculated by Rietveld refinement and foreign atom content, expressed as M at.%.

Sample	a (Å)	b (Å)	c (Å)	β (°)	V (Å3)	Metal content (at.%) Rietveld	Metal content (at.%) Analytical
DCPD	6.372	15.191	5.821	118.517	495.123	–	–
DCPD-Mn	6.366	15.173	5.809	118.559	492.834	7.1	7.3 ± 1.3
DCPD-Co	6.369	15.188	5.814	118.521	494.161	1.7	1.2 ± 0.1
DCPD-Sr	6.453	15.323	5.855	118.284	509.881	31.8	32.6 ± 1.2

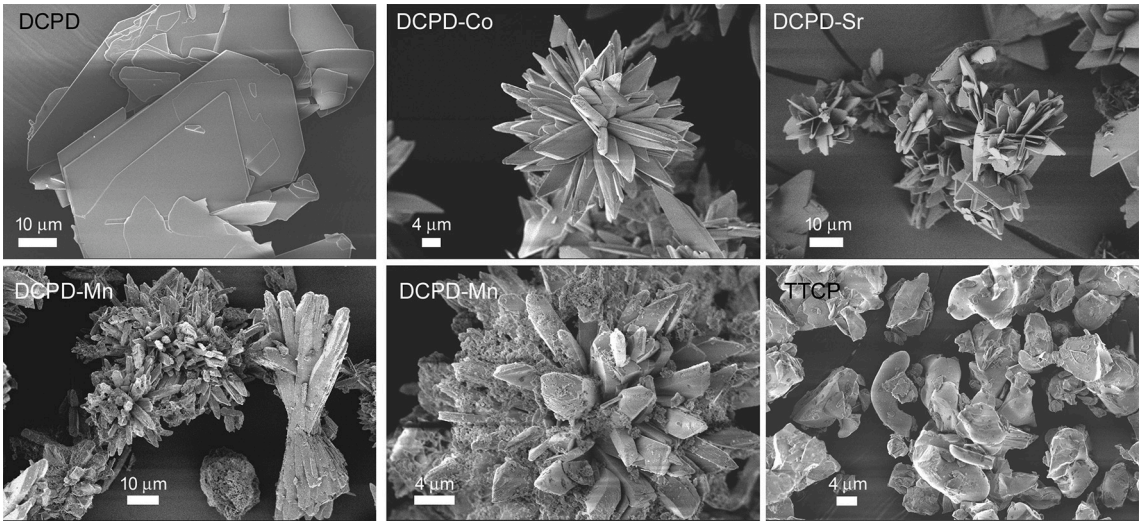

Fig. 2. SEM images of DCPD, DCPD-Co, DCPD-Mn, DCPD-Sr and TTCP powders.

instructions. The obtained cDNA was diluted to the final concentration of 5 ng/μL for each sample, taking into account the starting amount of RNA, to exploit the same range of amplification efficiency. Semi-quantitative polymerase chain reaction (PCR) analysis was performed for each sample, in duplicate, in LightCycler 2.0 Instrument (Roche Diagnostics GmbH, Manheim, Germany) using QuantiTect SYBR Green PCR Kit (Qiagen, Hilden, Germany) and gene-specific primers (**Table S1**). The protocol included a denaturation cycle at 95 °C for 15′, 25 to 40 cycles of amplification (95 °C for 15″, 55 °C annealing temperature for each target for 20″, and 72 °C for 20″). After melting curve analysis to check for amplicon specificity, the threshold cycle was determined for each sample, gene expression levels of the target genes were calculated by normalization to the reference gene GAPDH, using the comparative threshold method (ΔCt), [46]. The results were reported in terms of the number of molecules of the gene of interest per 100,000 molecules of the housekeeping gene GAPDH.

2.4. Statistical analysis

Statistical analysis was performed with GraphPad Prism software 9.5.1. Data are reported as mean ± standard deviations (SD) at a significance level of $p < 0.05$. After having verified normal distribution and homogeneity of variance, a two-way ANOVA was done for comparison between groups. Finally, the Sidak's *post hoc* multiple comparison test was performed to detect significant differences among groups.

3. Results and discussion

3.1. Powders characterization

Powder XRD patterns of DCPD synthesized in the presence of Co, Mn and Sr are compared with those of the product synthesized in the absence of foreign ions in Fig. 1. All the patterns are in agreement with the presence of DCPD as the only crystalline phase (ICDD PDF 00–009-0077). In particular, DCPD-Sr pattern shows a significant shift in the positions of the diffraction maxima, due to an appreciable variation of crystalline unit cell dimensions. Indeed, the values of the lattice constants calculated through structural refinement indicate an expansion of the unit cell of DCPD in the presence of Sr and a contraction in the presence of Mn and Co (Table 1). This is in agreement with previous findings [44] and with the different ionic radius of the foreign ions: bigger than that of Ca (0.112 nm) in the case of Sr (0.126 nm), and smaller for Co (0.90 nm) and Mn (0.96 nm).

The foreign ion content, determined through structural analysis (Table 1) is in good agreement with the results of the chemical analysis.

Scanning electron microscopy investigation highlights the different morphologies of the different powders (Fig. 2). SEM images of pure DCPD show the presence of big plate-like crystals characterized by large (010) faces. The presence of foreign ions induces crystals aggregation: in particular DCPD-Co appears constituted of clusters of thick, pointed crystals, whereas DCPD-Mn images show aggregates of almost cylindrical crystals. The crystals in DCPD-Sr aggregates exhibit a morphology more similar to that of pure DCPD, but much smaller dimensions. SEM images of TTCP show the presence of crystal blocks, characteristic of a solid-state reaction product (Fig. 2).

3.2. Materials characterization

The hardening process was investigated through X-ray diffraction analysis of the changes in the crystalline phase composition with time (Fig. 3). XRD patterns show a delaying effect of Co (b) and Mn (c) on the conversion of the crystalline mixture into the final apatitic phase: at variance with c-Ca, DCPD is still present in the materials containing Co and Mn after 1 day hardening, while the presence of Sr (d) has a lower inhibiting effect. The different influence of the different ions on the reactivity is even more remarkable when considering the relatively small contents of Co and Mn in comparison to that of Sr.

A semiquantitative analysis of phase composition was obtained through structural refinement of the XRD patterns of the materials after 8 h and 7 d hardening. The data reported in Table 2 indicate that the

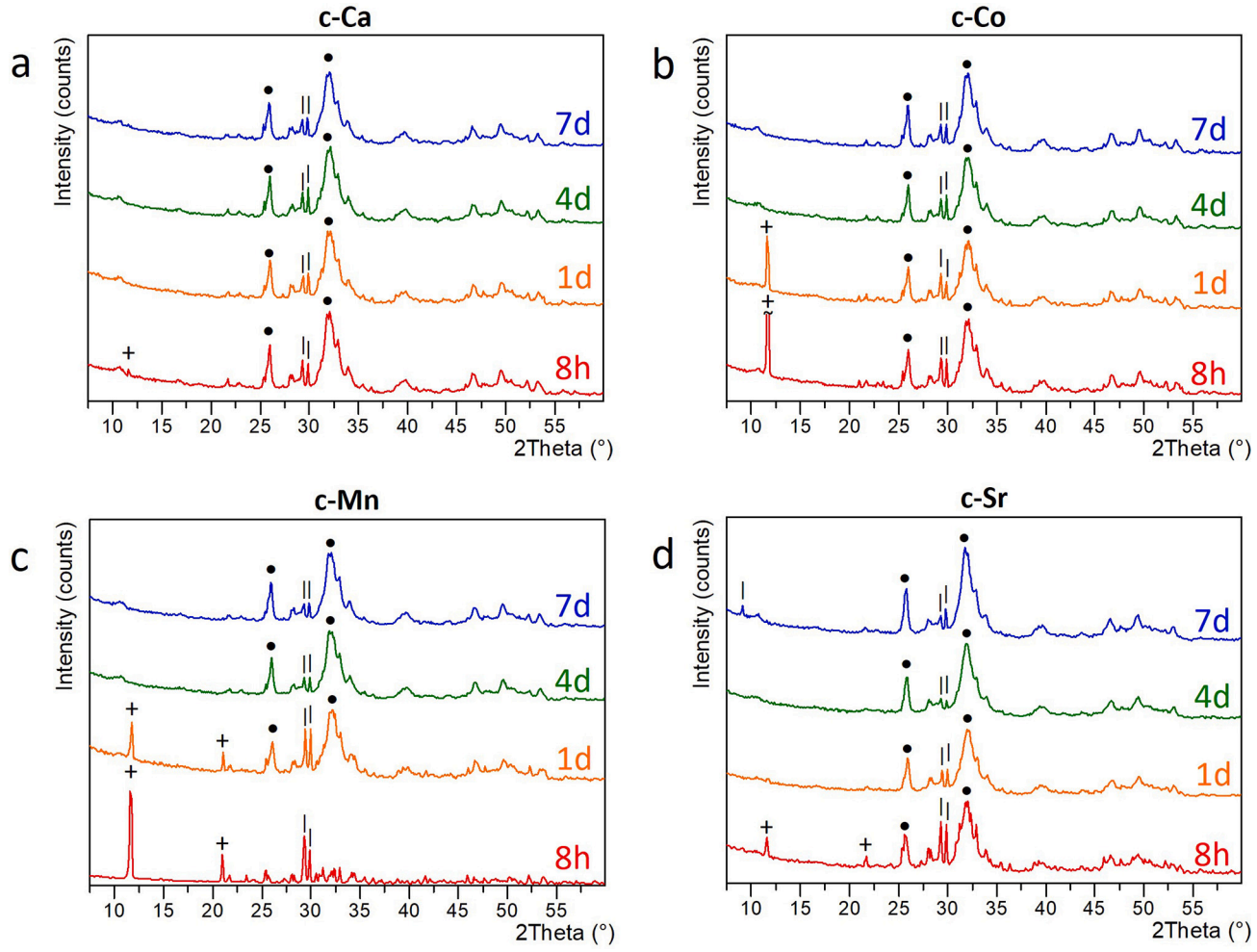

Fig. 3. Hardening kinetic of a) c-Ca; b) c-Co; c) c-Mn and d) c-Sr. Symbols •, HA [ICDD PDF 00-009-0432]; |, TTCP [ICDD PDF 01–070-1379] and +, DCPD [ICDD PDF 00–009-0077].

Table 2
Phase composition (%) of materials at different hardening times, before and after release in TRIS.

Hardening time	Sample	Before – Release				After – Release		
		DCPD	TTCP	HA*	R_{wp}	TTCP	HA*	R_{wp}
8 h	c-Ca	4	34	62	8.8	7	93	12.7
	c-Mn	27	69	4	10.8	26	74	9.4
	c-Co	10	35	55	8.1	6	94	9.9
	c-Sr	5	32	66	8.1	27	73	8.0
7 d	c-Ca	–	15	85	9.9	12	88	10.2
	c-Mn	–	15	85	10.5	14	86	9.9
	c-Co	–	17	83	10.2	17	83	9.4
	c-Sr	–	19	81	9.5	15	85	9.1

R_{wp}: Weighted profile residual.
When the fitting is not perfect, it could contain some amorphous phase.
* Phase fitted as HA [ICDD PDF 00–009-0432], although the phase has low crystallinity and wide peaks.

main component of all the samples after 7 days is poorly crystalline hydroxyapatite [ICDD PDF 00-009-0432], whereas some remaining TTCP [ICDD PDF 01-070-1379] accounts for <20 %. Samples hardened for just 8 h contain also unreacted DCPD [ICDD PDF 00-009-0077] in different amounts depending on the substituting ion. In agreement with their influence on the hydrolysis of DCPD [44], Sr displays just a mild inhibition of the conversion reaction, while the stronger delaying effect of Co and Mn provokes the presence of larger amounts of unreacted components. These findings are in agreement with previous data, which indicated that Mn delayed the formation of the final apatitic phase in a cement of different composition, and Co played an inhibiting role on the conversion of a brushitic cement [17,22]. On the other hand, it was reported that the involvement of strontium-substituted octacalcium phosphate in the composition of an apatitic cement did not greatly influence the process of phase conversion [47].

Phase composition was evaluated also after immersion of the disks in a Tris(hydroxymethyl)aminomethane 0.1 M solution for 7 days (Table 2) No significant variation of phase composition was appreciable for samples hardened for 7 days after immersion in TRIS. At variance, the compositions of the materials hardened for 8 h and then immersed in

Table 3
Foreign ion content of materials hardened for 8 h and 7 days. Data are expressed as $[M^{2+}/(Ca^{2+} + M^{2+})]\cdot 100$.

Hardening time	Sr content (at.%)	Co content (at.%)	Mn content (at.%)
8 h	15.25 ± 0.22	0.85 ± 0.01	4.61 ± 0.02
7 d	15.33 ± 0.13	0.80 ± 0.01	4.53 ± 0.07

TRIS for 7 days do not contain appreciable amounts of DCPD. Furthermore, they show a reduced content of TTCP: about 7 % for c-Ca and c-Co and about 27 % for c-Mn and c-Sr.

The foreign ion content of the different samples does not change significantly during hardening and is coherent with the starting compositions (Table 3). As expected, c-Sr has the highest content of foreign ion, about 15 at.% of Sr, whereas c-Co and c-Mn contain lower amounts of the foreign ions, about 0.8 and 4.5 at.% respectively.

Ionic release in TRIS solution is very modest, as shown in Figs. 4 and 5. The release of the foreign ions in saline is generally even lower than in TRIS solution, as shown in the graphs of release of the samples after 7d hardening reported in Fig. 4, most likely because of the different ionic strength. However, the release is related to the content of foreign ion in the material, with c-Sr showing the highest release followed by c-Mn and then c-Co. Moreover, c-Sr shows also the highest release of calcium (Fig. 5), in agreement with the increase of solubility of hydroxyapatite in the presence of strontium [48]. A very limited release of Mn in TRIS was previously reported for a brushitic cement [22], whereas greater amounts of Sr were reported to be released in TRIS from an apatitic cement [30]. As expected, the ionic release from 8 h samples, which have not completed their hardening, is significantly higher compared to 7d ones (**Figs. S1, S2**). However, also the samples hardened for 8 h show a metal ion release significantly higher for c-Sr in comparison to c-Mn and c-Co, in agreement with the different content of the materials. Again, Sr-containing samples release the highest amount of Ca, confirming a higher solubility of c-Sr.

Fig. 6 reports SEM images of the surfaces of the materials after 7 days hardening. The surfaces appear quite compact, although the shape of several pristine brushite crystals can be appreciated, especially in the case of c-Co and c-Mn. Images at higher magnification reveal the presence of entanglements of small plate-like crystals in c-Ca, whereas the structures obtained in the presence of foreign ions appear more compact (Fig. 6). Micrographs of the cross-sections (Fig. 7) confirm the greater presence of the pristine brushite crystals in the images from c-Co and c-Mn, and put into evidence the presence of entangled small plate-like crystals in all the materials.

Surfaces of materials hardened for 8 h (Fig. S3) appear slightly less compact than samples hardened for 7 days, while cross-section images (Fig. S3) show the onset of the crystals entanglement.

The values of open porosity reported in Fig. 8 indicate that the materials containing foreign ions generally display a reduced porosity than c-*Ca.*

The mechanical properties are also influenced by the presence of doping ions: the materials obtained using substituted DCPD exhibit significantly higher compressive strength than c-*Ca.* (Fig. 8). This could be related to the smaller values of open porosity and/or to variations in crystal size and consequent crystal entanglement.

The differences in the structural organization of the scanned materials are clearly visible from the 2D cross-section images and 3D

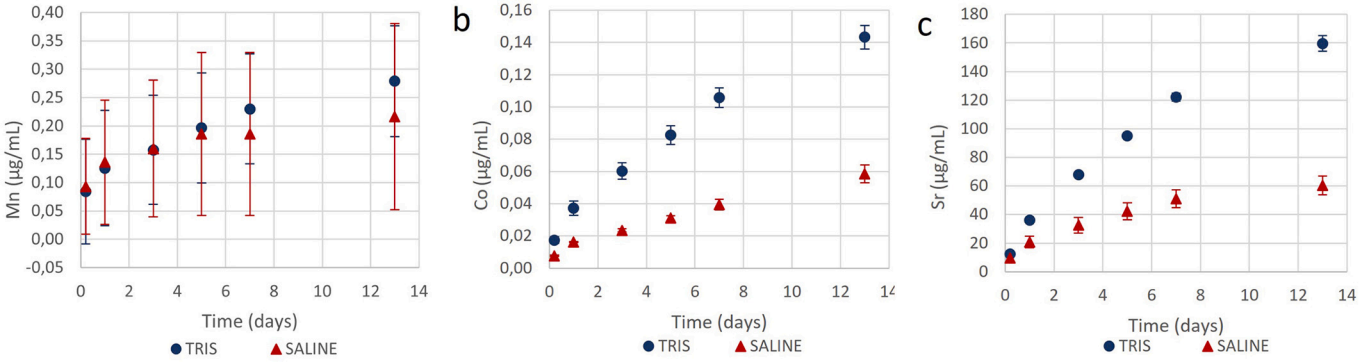

Fig. 4. Ion release in TRIS and saline solutions from 7d cements: (a) c-Mn, (b) c-Co and (c) c-Sr.

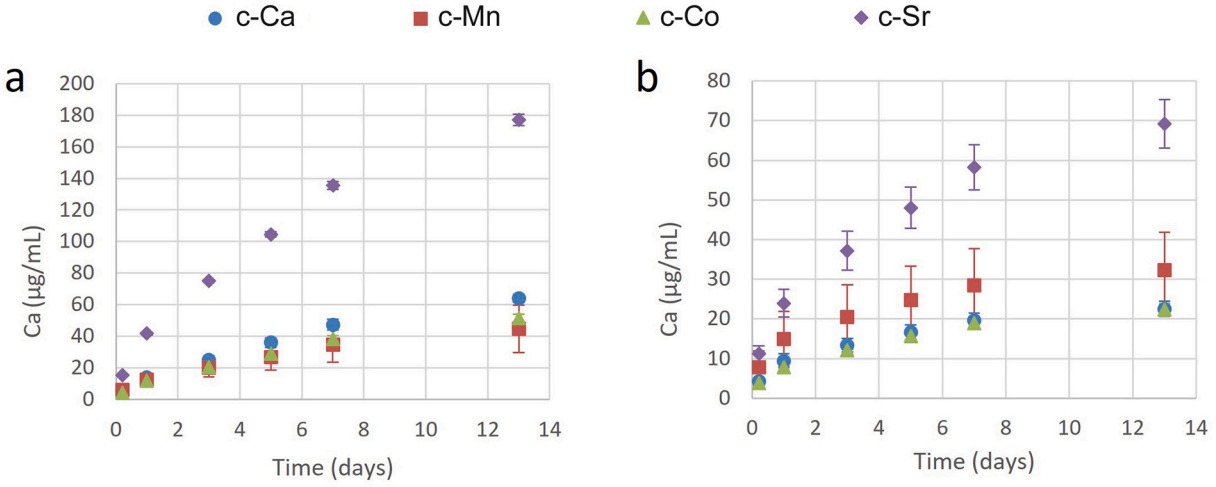

Fig. 5. Comparison of calcium release in TRIS (a) and Saline (b) from cements hardened 7 days.

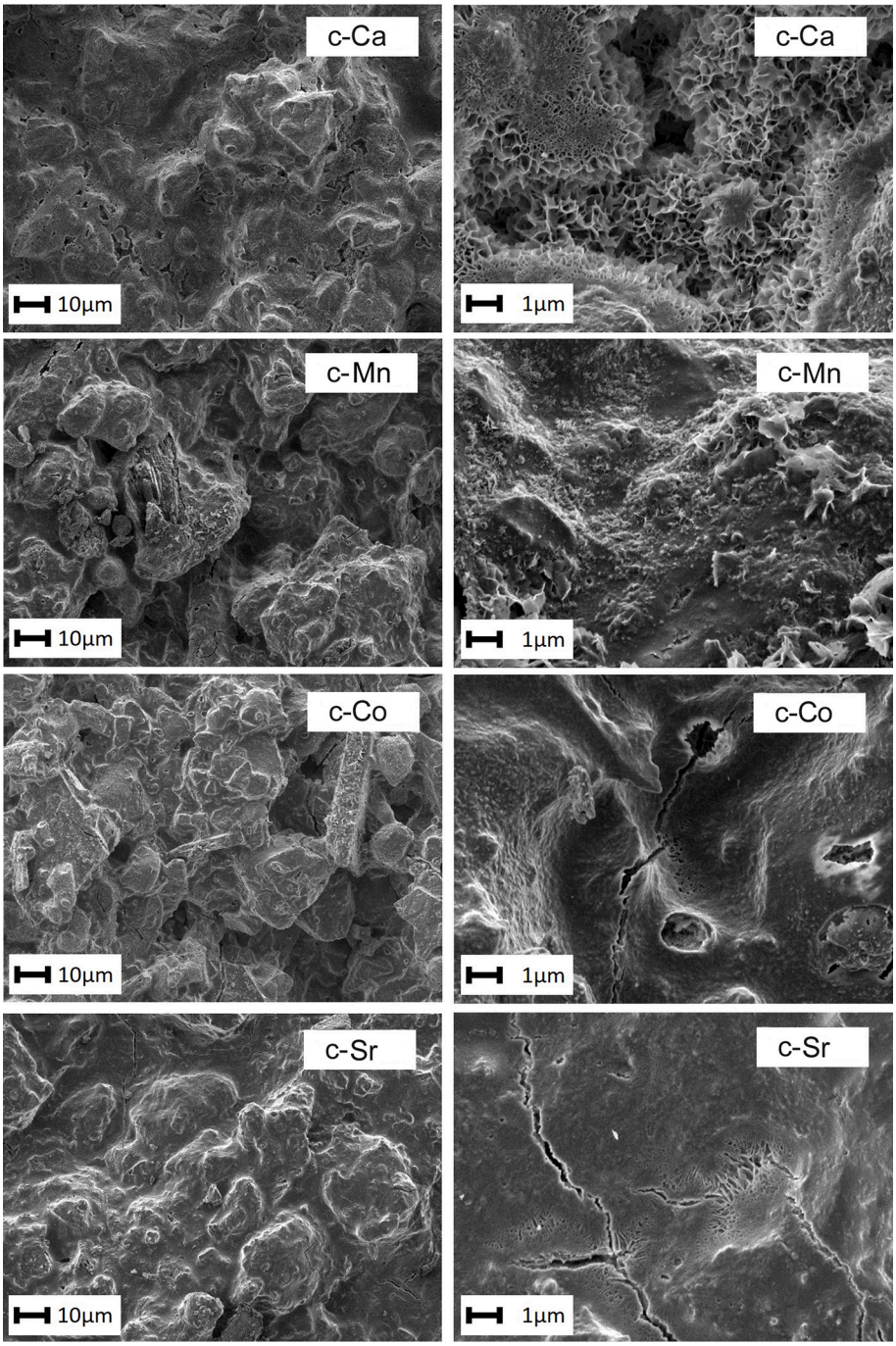

Fig. 6. Scanning electron micrographs of the surfaces of 7 d disks of c-Ca, c-Mn, c-Co, and c-Sr. Lower magnifications on the left; higher magnifications on the right.

reconstructed VOI. The 3D renderings show differences in the morphology of the samples, with a more homogeneous structure in c-Mn, c-Co, c-Sr in comparison c-Ca sample, which has a more discontinuous and irregular surface (Fig. 9). The values of total porosity confirm the trend observed for open porosity (Fig. 8): the highest value of total porosity was observed in c-Ca (50.03 ± 1.6 %), whereas smaller values were found for c-Co (48.2 ± 2 %), c-Mn (47.3 ± 1.6 %) and c-Sr (46.5 ± 1.5 %).

3.3. Biological tests

3.3.1. Cell viability

A clear difference among experimental materials emerged from cell metabolic activity assay. All materials increased over time their metabolic activity, but the highest value was reached by the cells grown in direct contact with c-Mn and c-Sr, which showed a significant high metabolic activity than those grown in direct contact with c-Co and c-Ca, at both 7 and 14 days (Fig. 10). These differences are clearly due to the presence of Mn and Sr.

3.3.2. Quantitative polymerase chain reaction (qPCR)

After 3, 7 and 14 days of culture, the expression of *OSTERIX, RUNX2, COL1A1, OPG/RANKL, ALP, BGLAP, vWF* and *VEGF* was differently stimulated from the different materials.

OSTERIX (Sp7 transcription factor) is a master gene that regulate the expression of a set of extracellular matrix proteins, *e.g.*, osteocalcin and collagen type-I, also involved in BMP-induced terminal osteoblast differentiation [49,50]. Its expression was significantly higher at 3 days

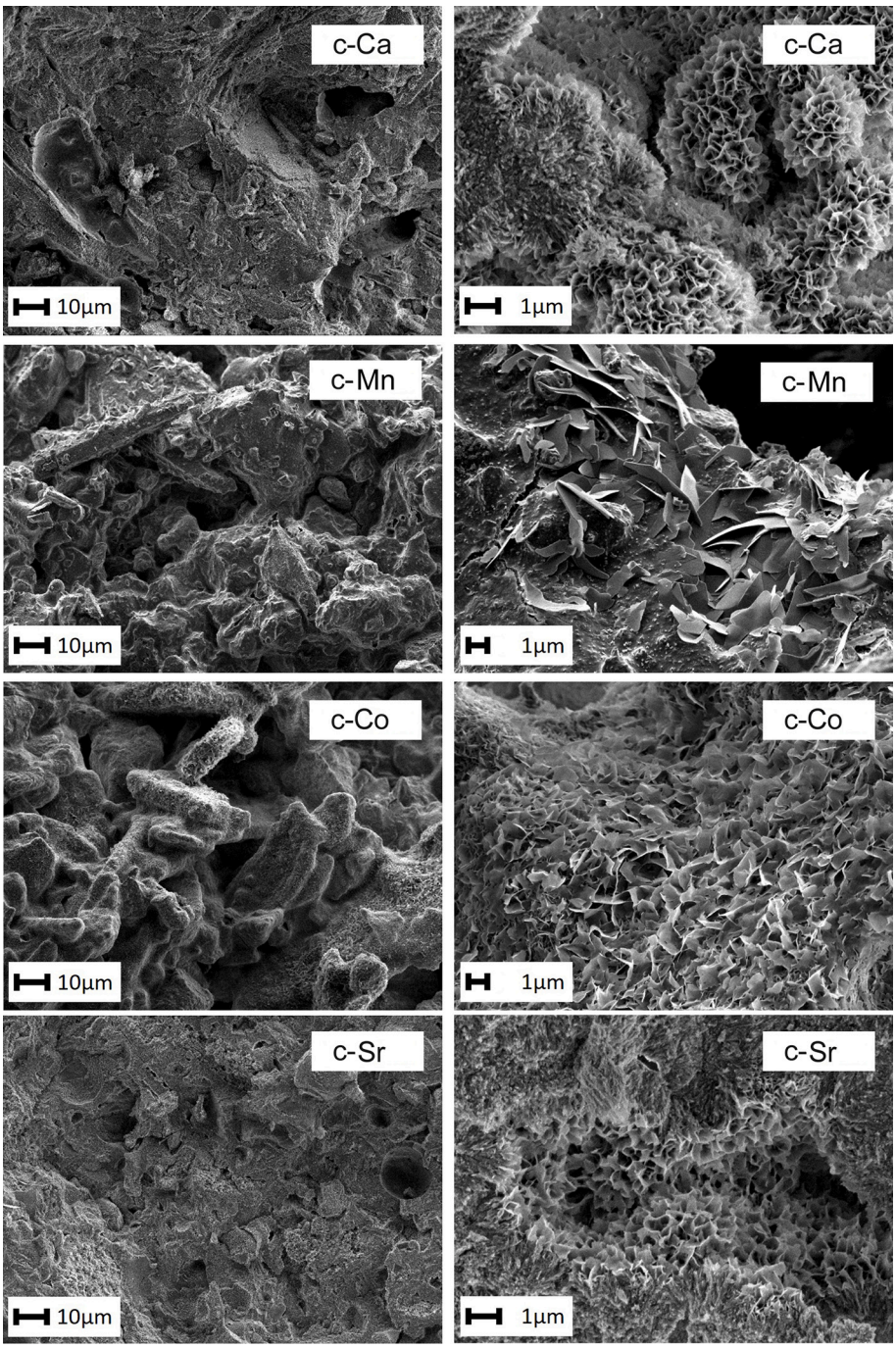

Fig. 7. SEM images of the cross-sections of 7 d disks of c-Ca, c-Mn, c-Co, and c-Sr. Lower magnifications on the left; higher magnifications on the right.

than at 7 and 14 days on c-Mn material and at 3 days in comparison to 7 days on c-Ca material (Fig. 11A). In addition, at 3 days *OSTERIX* expression showed significant lower values on c-Co, c-Sr and c-Ca than on c-Mn (Fig. 11A). Significant differences between materials were detected also for the expression of RUNX family transcription factor 2 (*RUNX2)* [51,52], an essential regulator of the osteoblastic function (Fig. 11B). Gene expression at 3 days for each material was statistically significantly higher than at the other experimental times, except on c-Co, which showed the lowest value; the highest expression level was recorded on c-Ca at 3 days (Fig. 11B). *RUNX2* can interact with *OSTERIX* to coordinately induce the expression of the collagen type I alpha 1 chain (*COL1A1)* gene encoding the main component of collagen type I. The level of *COL1A1* significantly increased over time on c-Mn and c-Sr while the values on c-Co were the lowest at each experimental time (Fig. 11C).

In addition to COL1A1, *RUNX2* also controls the expression of alkaline phosphatase (*ALP)* and bone gamma-carboxyglutamate protein (*BGLAP)* [53]. In particular, *ALP*, a cell surface protein ubiquitously expressed by several cell types, is used as marker for screening pre-osteoblasts. The highest *ALP* expression values were obtained on c-Mn at 7 days and 14 days, although with different level of significance, while the lowest values were recorded on c-Co at each experimental time (Fig. 12A). In addition to *ALP,* a late differentiation marker associated with bone mineralization and matrix synthesis is represented by *BGLAP/* osteocalcin, a small conserved non-collagenous extracellular matrix protein [54]. *BGLAP* showed significant lower expression at all experimental times on c-Co materials *versus* c-Mn, c-Sr and c-Ca (Fig. 12B).

The homeostasis of bone metabolism is maintained by the balance between osteoblast bone formation and osteoclast bone resorption, and

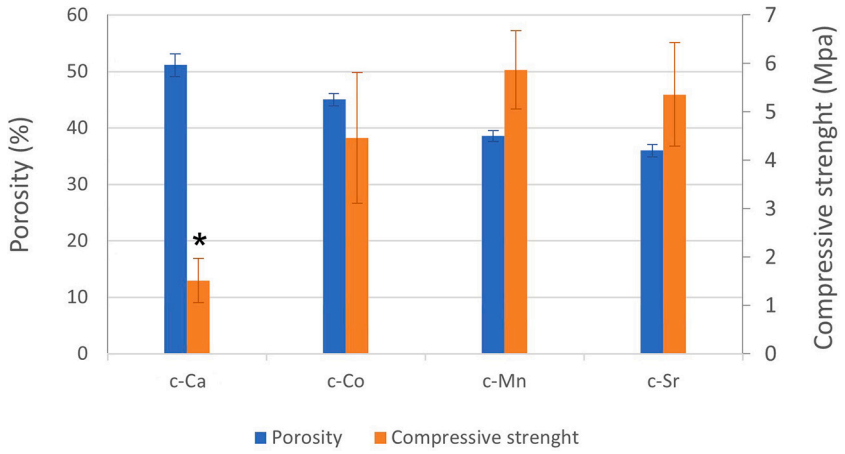

Fig. 8. Values of open porosity (%) as determined by MIP and compressive strength of the different materials after 7 days hardening. Results are the average over 12 measurements. * c-Ca *vs.* c-Co, c-Mn, c-Sr ($p < 0.01$).

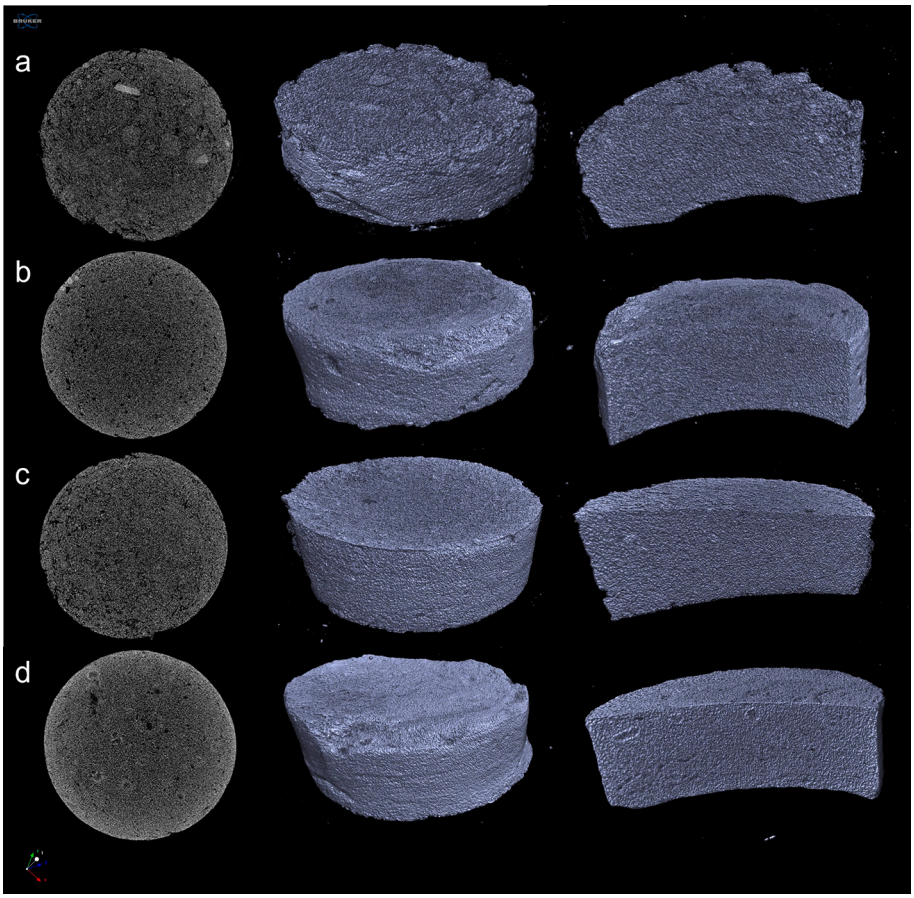

Fig. 9. Dataset reconstructions of c-Ca (a), c-Mn (b), c-Co (c), c-Sr (d) samples. Visualization of a cross section in the transverse plane (first column) and 3 d renderings (second and third columns) of representative samples.

the relative levels of TNF receptor superfamily member 11b (*OPG)* and TNF superfamily member 11 (*RANKL)* determine the processes of osteogenesis and osteoclastogenesis [55,56]. *RANKL*, produced by osteoblasts, induces osteoclast differentiation by binding to its receptor, *RANK*. Osteoblasts also produce the soluble protein *OPG*, which blocks the interaction between *RANKL* and *RANK*, and thus controls the process of bone metabolism. The *ratio* between these two bone markers (*OPG/RANKL*) reflects the balance between the stimulus in promoting bone formation (*OPG*) and that related to bone absorption (*RANKL*). The ratio between these markers suggested that the predominant activity is towards bone formation for all the investigated materials: in particular at 7 days when the number of molecules obtained for *OPG* was much higher than that of *RANKL* molecules, suggesting that these innovative materials reduce the expression of RANKL (Fig. 13). At 7 days c-Sr showed the highest OPG/RANKL *ratio,* thus exhibiting also the highest potential ability to prevent osteoclastic activation.

Finally, vascular endothelial growth factor (*VEGF*), which is the master regulator of blood vessel growth and the key molecular target of

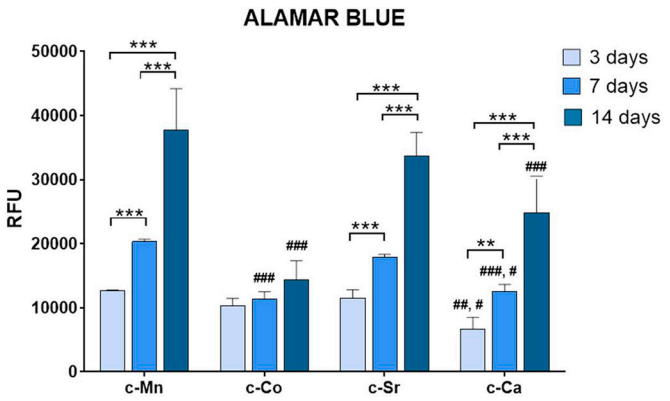

Fig. 10. Cell viability determined by alamar blue staining of hMSCs grown in direct contact with materials after 3 days 7 and 14 days. The results are given as relative fluorescent units and statistical analysis is reported in the graphs (between experimental times in the same material: *** $p < 0.0005$; among experimental materials in the same experimental time: ### $p < 0.0005$; ## $p < 0.005$; # $p < 0.05$;). Between experimental time in the same material: c-Mn *** 3 days *vs.* 7 days, 3- and 7- days *vs.* 14 days; c-Sr *** 3 days *vs.* 7 days, 3- and 7- days *vs.* 14 days; c-Ca *** 3 days *vs.* 7 days, 3- and 7- days *vs.* 14 days. Among experimental materials in the same experimental time: 3 days ## c-Ca *vs* c-Mn and # c-Ca *vs* c-Sr; 7 days ### c-Ca *vs.* c-Mn and # c-Ca *vs* c-Sr; 7 days ### c-Co *vs.* c-Mn and c-Sr; 14 days ### c-Ca *vs.* c-Mn and c-Sr and ### c-Co *vs.* c-Mn, c-Sr and c-*Ca.*

strategies to promote vascular network expansion, showed its peak in all tested materials at 3 days while a progressive reduction was detected at 7 and 14 days (Fig. 14A). This trend is particularly important since studies have shown that neovascularization around the material before bone formation could provide blood supply for the subsequent osteogenic differentiation [57]. Furthermore, it is well known that *VEGF* acts early during vessel formation. Differently, vWF showed significantly higher values at all experimental time points for c-Mn compared to all other tested materials (Fig. 14B). vWF serves as a multifunctional protein that facilitates endothelial cell adhesion, platelet recruitment, angiogenic signaling, and regulation of blood flow, all of which are critical for the process of angiogenesis.

Although VEGF and vWF have distinct functions and mechanisms of action, both play a key role in angiogenesis. VEGF, as previously mentioned, is known to be one of the key mediators of angiogenesis, while vWF, on the other hand, is involved in blood clotting and platelet adhesion, but can also be secreted by endothelial cells during angiogenesis to facilitate the formation of new vessels.

4. Conclusions

The examined foreign ions display different effects on the obtained apatitic materials. Both Mn and Co ions exert a delaying role on the cementitious reaction between DCPD and TTCP. On the other hand, all the three foreign ions slightly reduce open and total porosity and enhance the compressive strength of the final apatitic materials. Since the cells are seeded in direct contact with the materials, they are significantly influenced by the foreign ions, although their ionic release

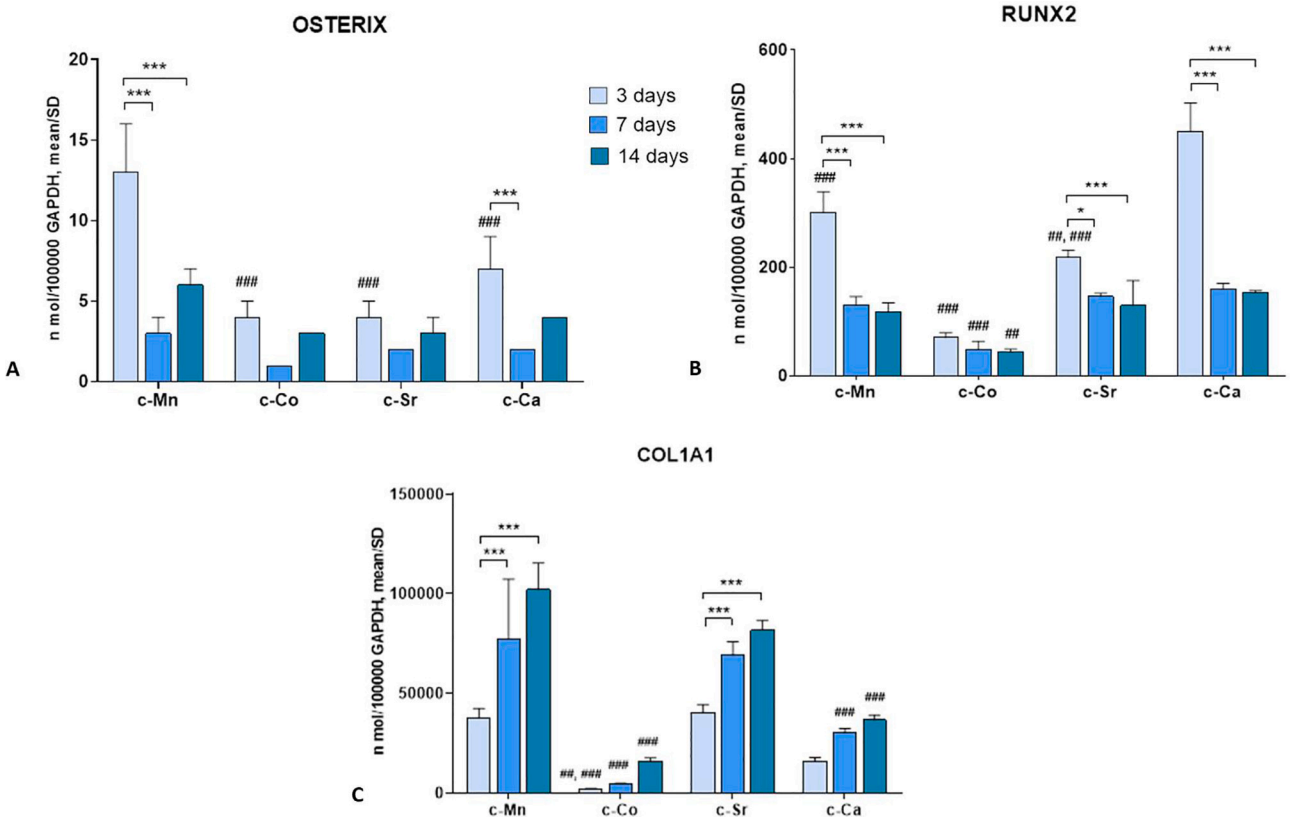

Fig. 11. Gene expression of *OSTERIX* (**A**), *RUNX2* (**B**) and *COL1A1* (**C**) after 3, 7 and14 days of culture of hMSC on presence c-Mn, c-Co, c-Sr and c-Ca materials. Statistical analysis is reported in the figure (*$p < 0.05$, ## $p < 0.005$, *** and ### $p < 0.0005$). Between experimental times in the same material: **OSTERIX**: c-Mn *** 3 days *vs* 7 and 14 days; c-Ca *** 3 days *vs* 7 days. **RUNX2:** c-Mn *** 3 days *vs* 7 and 14 days; c-Sr * 3 days *vs* 7 and *** 3 days *vs* 14 days; c-Ca *** 3 days *vs* 7 and 14 days; **COL1A1:** c-Mn *** 7 days *vs* 3 days and *** 14 days *vs* 3 days. Among experimental materials in the same experimental time: ***OSTERIX***: 3 days ### c-Co, c-Sr and c-Ca *vs.* c-Mn, **RUNX2**: 3 days ### c-Co *vs.* c-Mn, c-Sr and c-Ca; ## c-Sr *vs.* c-Mn; ### c-Sr and c-Mn *vs* c-Ca 7 days ### c-Co *vs.* c-Mn, c-Sr and c-Ca; 14 days ### c-Co *vs.* c-Mn, c-Sr and c-*Ca.* **COL1A1:** 3 days ### c-Co *vs.* c-Sr and ## c-Co *vs* c-Mn; 7 days ### c-Ca *vs* c-Mn and c-Sr and ### c-Co *vs* c-Mn and c-Sr; 14 days ### c-Co *vs.* c-Mn and ### c-Ca *vs* c-Sr. c-Mn.

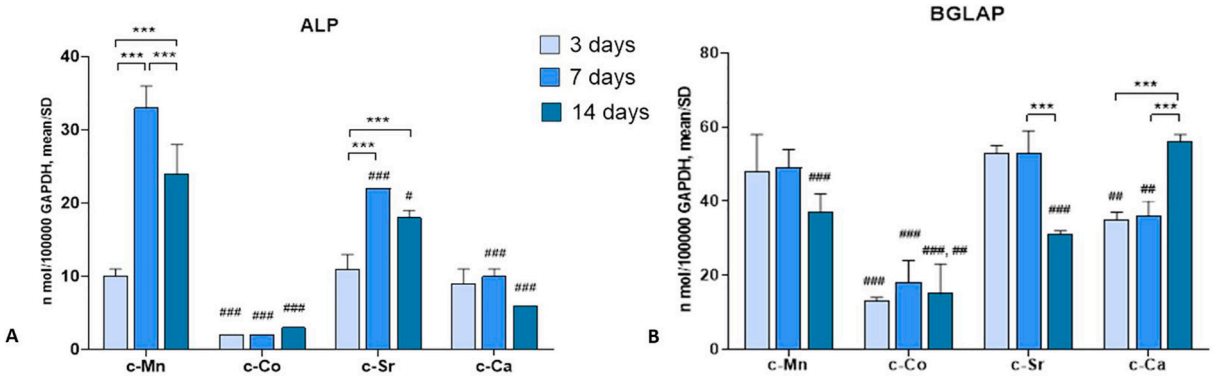

Fig. 12. Gene expression of *ALP* (**A**) and *BGLAP* (**B**) after 3, 7 and14 days of culture of hMSC on materials. Statistical analysis is reported in the figure ($^{\#}$ $p < 0.05$, ** and $^{\#\#}$ $p < 0.005$, *** and $^{\#\#\#}$ $p < 0.0005$). Between experimental times in the same material: **ALP**: c-Mn *** 7 days *vs.* 3 and 14 days; c-Sr *** 7 days and 14 days *vs.* 3 days. **BGLAP**: c-Sr *** 7 days *vs* 14 days; c-Ca *** 14 day *vs.* 3 and 7 days. Among experimental materials in the same experimental time **ALP**: 3 days $^{\#\#}$ c-Co *vs.* c-Mn, c-Sr and c-Ca; 7 days: $^{\#\#\#}$ c-Co *vs.* c-Mn, c-Sr and c-Ca and $^{\#\#\#}$ c-Sr *vs.* c-Mn and $^{\#\#\#}$ c-Ca *vs* c-Sr, c-Mn. **BGLAP**: 3, 7 and 14 days $^{\#\#\#}$ c-Co *vs.* c-Mn, c-Sr and c-Ca and $^{\#\#}$ c-Ca *vs* c-Sr; 14 days: $^{\#\#\#}$ c-Mn and c-Sr *vs* c-*Ca.*

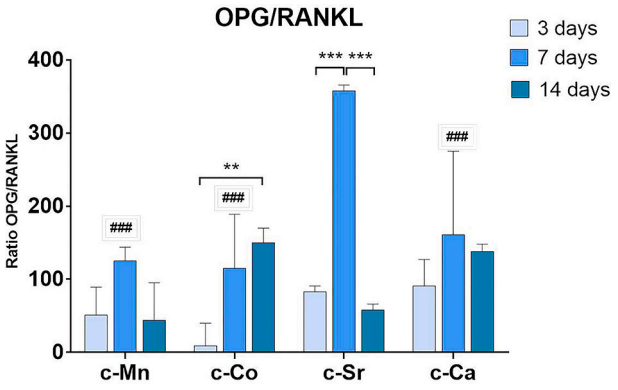

Fig. 13. Gene expression of *OPG/RANKL ratio* after 3, 7 and14 days of culture of hMSC on materials. Statistical analysis is reported in the figure (** $p < 0.005$, *** and $^{\#\#\#}$ $p < 0.0005$). Between experimental times in the same material: c-Co *** 3 days *vs.* 14 days; c-Sr *** 7 days *vs.* 3 and 14 days. Among experimental materials in the same experimental time: 7 days$^{\#\#\#}$: c-Sr *vs.* c-Mn, c-Co and c-*Ca.*

in solution is modest. The higher values of c-Mn, c-Sr and c-Ca in term of viability is a sign of a greater proliferative stimulus in comparison to that exerted by c-Co, which shows a minor metabolic activity especially at 7 and 14 days. In summary, the biological results contribute to understand how the new synthesized materials interact with hMSCs, stimulating or inhibiting their activities. c-Mn, c-Sr and also c-Ca stimulate hMSCs osteoblastic activity, as showed by *OSTERIX, RUNX2, COL1A1, ALP* and *BGLAP* gene expression. Concerning *OPG/RANKL* the c-Sr material proves to be the most effective in regulating bone resorption by reducing the differentiation of preosteoclasts into osteoclasts. Another crucial determinant influencing osteoblastic activity is angiogenesis, the process of new blood vessel development, which is essential for meeting the nutritional requirements of new bone growth. In the current study, all materials stimulate human mesenchymal stem cells (hMSCs) to release both VEGF and vWF. However, the c-Mn material exhibits higher vWF values. VEGF and vWF are two factors capable of synergistically interacting or reciprocally regulating each other in the cellular environment, influencing their expression or secretion by MSCs. This interaction can promote both angiogenesis and tissue regeneration, thereby facilitating cell adhesion and interaction with the surrounding microenvironment. On the basis of the whole data, c-Sr seems to be the best material since it displays a synergistic effect on osteogenesis, osteoclastogenesis and angiogenesis.

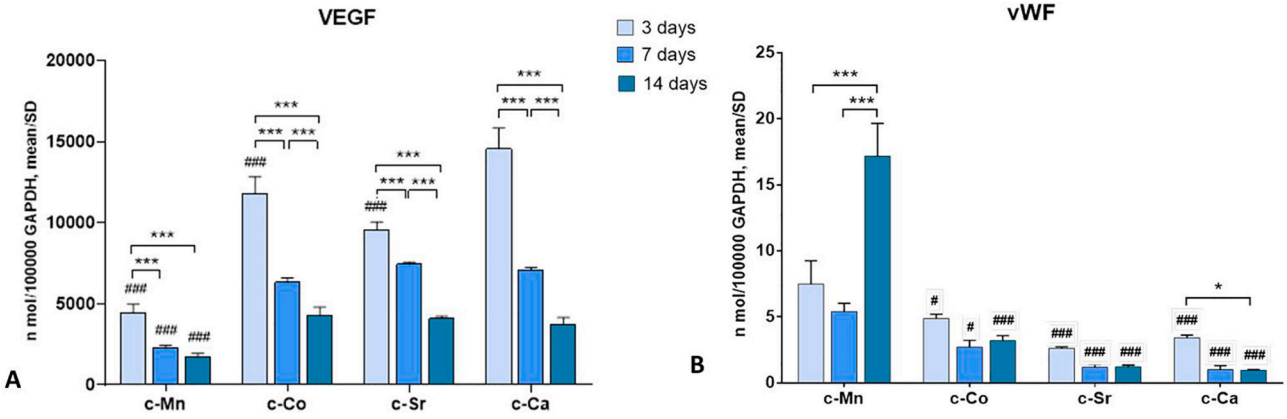

Fig. 14. Statistical analysis is reported in the figure *** and ### $p < 0.0005$). Between experimental time in the same material VEGF: c-Mn *** 3 days *vs.* 7 and 14 days; c-Co *** 3 days *vs.* 14 days and 7 days *vs.* 14 days; c-Sr *** 3 days *vs.* 14 days and 7 days *vs.* 14 days; c-Ca *** 3 days *vs.* 14 days and 7 days *vs.* 14 days; vWF:c-Mn *** 14 days *vs* 7 and 3 days; c-Ca *** 3 days *vs 14* days. Among experimental materials in the same experimental time VEGF: 3 days $^{\#\#\#}$ c-Mn, c-Co and c-Sr *vs* c-Ca and $^{\#\#\#}$ c-Mn and c-Sr *vs* c-Co; 7 days $^{\#\#\#}$ c-Mn *vs.* c-Co, c-Sr and c-Ca; 14 days$^{\#\#\#}$ c-Mn *vs.* c-Co, c-Sr and c-Ca; vWF: 3 days: c-Co *vs* c-Mn ($^{\#}$: $p < 0.05$) and C—Sr and c-Ca *vs* c-Mn ($^{\#\#\#}$: $p < 0.0005$); 7 days: c-Co *vs* c-Mn (#: p < 0.05) and C—Sr and c-Ca *vs* c-Mn (###: p < 0.0005); 14 days: c-Co, C—Sr and C—Ca *vs* c-Mn ($^{\#\#\#}$: $p < 0.0005$).

CRediT authorship contribution statement

Francesca Salamanna: Writing – review & editing, Writing – original draft, Validation, Methodology, Investigation, Formal analysis, Data curation. **Montserrat Español:** Writing – review & editing, Validation, Methodology, Investigation, Data curation. **Melania Maglio:** Methodology, Investigation, Data curation. **Maria Sartori:** Methodology, Investigation, Data curation. **Gianluca Giavaresi:** Validation, Supervision, Resources. **Adriana Bigi:** Writing – review & editing, Writing – original draft, Validation, Supervision, Conceptualization. **Maria-Pau Ginebra:** Writing – review & editing, Supervision, Resources, Conceptualization. **Elisa Boanini:** Writing – review & editing, Writing – original draft, Supervision, Resources, Project administration, Methodology, Funding acquisition, Conceptualization.

Declaration of competing interest

The authors declare that they have no known competing financial interests or personal relationships that could have appeared to influence the work reported in this paper.

Data availability

Data will be made available on request.

Acknowledgments

The authors kindly acknowledge the University of Bologna (Marco Polo programme) and the Spanish Ministry of Science, Innovation and Universities for financial support through the PID2019-103892RB-I00/AEI/10.13039/501100011033 project. MPG acknowledges the Generalitat de Catalunya for the ICREA Academia Award.

Appendix A. Supplementary data

Supplementary data to this article can be found online at https://doi.org/10.1016/j.bioadv.2024.213968.

References

[1] E. Boanini, M. Gazzano, A. Bigi, Ionic substitutions in calcium phosphates synthesized at low temperature, Acta Biomater. 6 (2010) 1882–1894, https://doi.org/10.1016/j.actbio.2009.12.041.
[2] S.V. Dorohzkin, Calcium orthophosphates (CaPO4): occurrence and properties, Prog. Biomater. 5 (2016) 9–70, https://doi.org/10.1007/s40204-015-0045-z.
[3] A. Laskus, J. Kolmas, Ionic substitutions in non-apatitic calcium phosphates, Int. J. Mol. Sci. 18 (2017) 2542, https://doi.org/10.3390/ijms18122542.
[4] V. Uskoković, Ion-doped hydroxyapatite: an impasse or the road to follow? Ceram. Int. 46 (Part B) (2020) 11443–11465, https://doi.org/10.1016/j.ceramint.2020.02.001.
[5] M.C. Tronco, J.B. Cassel, L. dos Santos, α-TCP-based calcium phosphate cements: a critical review, Acta Biomater. 151 (2022) 70–87, https://doi.org/10.1016/j.actbio.2022.08.040.
[6] I. Lodoso-Torrecilla, J.J.J.P. van den Beucken, J.A. Jansen, Calcium phosphate cements: optimization toward biodegradability, Acta Biomater. 119 (2021) 1–12, https://doi.org/10.1016/j.actbio.2020.10.013.
[7] W.E. Brown, L.C. Chow, A new calcium phosphate water setting cement, in: P. W. Brown (Ed.), Cements Research Progress, American Ceramic Society, Westerville, OH, 1986, pp. 352–379.
[8] M.P. Ginebra, C. Canal, M. Espanol, D. Pastorino, E.B. Montufar, Calcium phosphate cements as drug delivery materials, Adv. Drug Deliv. Rev. 64 (2012) 1090–1110, https://doi.org/10.1016/j.addr.2012.01.008.
[9] A. Sugawara, K. Asaoka, S.J. Ding, Calcium phosphate-based cements: clinical needs and recent progress, J. Mater. Chem. B 1 (2013) 1081–1089, https://doi.org/10.1039/C2TB00061J.
[10] J. Zhang, W. Liu, V. Schnitzler, F. Tancret, J.M. Bouler, Calcium phosphate cements for bone substitution: chemistry, handling and mechanical properties, Acta Biomater. 10 (2014) 1035–1049, https://doi.org/10.1016/j.actbio.2013.11.001.
[11] G. Mestres, M.P. Ginebra, Novel magnesium phosphate cements with high early strength and antibacterial properties, Acta Biomater. 7 (2011) 1853–1861, https://doi.org/10.1016/j.actbio.2010.12.008.
[12] S.V. Dorohzkin, Self-setting calcium orthophosphate formulations, J. Funct. Biomater. 4 (2013) 209–311, https://doi.org/10.3390/jfb4040209.
[13] C. Mellier, F. Fayon, F. Boukhechba, E. Verron, M. LeFerrec, G. Montavon, J. Lesoeur, V. Schnitzler, D. Massiot, P. Janvier, O. Gauthier, J.M. Bouler, B. Bujoli, Design and properties of novel gallium-doped injectable apatitic cements, Acta Biomater. 24 (2015) 322–332, https://doi.org/10.1016/j.actbio.2015.05.027.
[14] A. Lode, C. Heiss, G. Knapp, J. Thomas, B. Nies, M. Gelinsky, M. Schumacher, Strontium-modified premixed calcium phosphate cements for the therapy of osteoporotic bone defects, Acta Biomater. 65 (2018) 475–485, https://doi.org/10.1016/j.actbio.2017.10.036.
[15] K. Spaeth, F. Goetz-Neunhoeffer, K. Hurle, The effect of Cu2+ doping in β-tricalcium phosphate on the hydration mechanism of a brushite cement, Mater. Today Chem. 27 (2023) 101288, https://doi.org/10.1016/j.mtchem.2022.101288.
[16] A. Bigi, E. Boanini, M. Gazzano, Ion substitution in biological and synthetic apatites, in: C. Aparicio, M.P. Ginebra (Eds.), Biomineralization and Biomaterials: Fundamentals and Applications, Woodhead Publishing (Elsevier), Cambridge, UK, 2016, pp. 235–266, https://doi.org/10.1016/B978-1-78242-338-6.00008-9.
[17] H. Cummings, W. Han, S. Vahabzadeh, S.F. Elsawa, Cobalt-doped brushite cement: preparation, characterization, and in vitro interaction with osteosarcoma cells, JOM 69 (2017) 1348–1353, https://doi.org/10.1007/s11837-017-2376-9.
[18] T. Tian, Y. Han, B. Ma, C. Wu, J. Chang, Novel Co-akermanite ($Ca_2CoSi_2O_7$) bioceramics with the activity to stimulate osteogenesis and angiogenesis, J. Mater. Chem. B 3 (2015) 6773–6782, https://doi.org/10.1039/C5TB01244A.
[19] J. Zhou, L. Zhao, Hypoxia-mimicking Co doped TiO2 microporous coating on titanium with enhanced angiogenic and osteogenic activities, Acta Biomater. 43 (2016) 358–368, https://doi.org/10.1016/j.actbio.2016.07.045.
[20] S. Kulanthaivel, B. Roy, T. Agarwal, S. Giri, K. Pramanik, K. Pal, S.S. Ray, T. K. Maiti, I. Banerjee, Cobalt doped proangiogenic hydroxyapatite for bone tissue engineering application, Mater. Sci. Eng. C Mater. Biol. Appl. 58 (2016) 648–658, https://doi.org/10.1016/j.msec.2015.08.052.
[21] A. Bernhardt, M. Schamel, U. Gbureck, M. Gelinsky, Osteoclastic differentiation and resorption is modulated by bioactive metal ions Co^{2+}, Cu^{2+} and Cr^{3+} incorporated into calcium phosphate bone cements, PLoS One 12 (2017) e0182109, https://doi.org/10.1371/journal.pone.0182109.
[22] T. Wu, H. Shi, Y. Liang, T. Lu, Z. Lin, J. Ye, Improving osteogenesis of calcium phosphate bone cement by incorporating with manganese doped β-tricalcium phosphate, Mater. Sci. Eng. C Mater. Biol. Appl. 109 (2020) 110481, https://doi.org/10.1016/j.msec.2019.110481.
[23] I. Mayer, O. Jacobsohn, T. Niazov, J. Werckmann, M. Iliescu, M. Richard-Plouet, O. Burghaus, D. Reinen, Manganese in precipitated hydroxyapatites, Eur. J. Inorg. Chem. 2003 (2003) 1445–1451, https://doi.org/10.1002/ejic.200390188.
[24] B. Bracci, P. Torricelli, S. Panzavolta, E. Boanini, R. Giardino, A. Bigi, Effect of Mg^{2+}, Sr^{2+}, and Mn^{2+} on the chemico-physical and in vitro biological properties of calcium phosphate biomimetic coatings, J. Inorg. Biochem. 103 (2009) 1666–1674, https://doi.org/10.1016/j.jinorgbio.2009.09.009.
[25] C. Paluszkiewicz, A. Ślósarczyk, D. Pijocha, M. Sitarz, M. Bućko, A. Zima, A. Chróścicka, M. Lewandowska-Szumieł, Synthesis, structural properties and thermal stability of Mn-doped hydroxyapatite, J. Mol. Struct. 976 (2010) 301–309, https://doi.org/10.1016/j.molstruc.2010.04.001.
[26] W. Acchar, E.G. Ramalho, Effect of MnO_2 addition on sintering behavior of tricalcium phosphate: preliminary results, Mater. Sci. Eng. C Mater. Biol. Appl. 28 (2008) 248–252, https://doi.org/10.1016/j.msec.2006.12.011.
[27] G. Karunakaran, E.B. Cho, K. Thirumurugan, G.S. Kumar, E. Kolesnikov, S. Boobalan, G. Janarthanan, M.M. Pillai, S. Rajendran, Mesoporous Mn-doped hydroxyapatite nanorods obtained via pyridinium chloride enabled microwave-assisted synthesis by utilizing *Donax variabilis* seashells for implant applications, Mater. Sci. Eng. C Mater. Biol. Appl. 126 (2021) 112170, https://doi.org/10.1016/j.msec.2021.112170.
[28] P.J. Marie, P. Ammann, G. Boivin, C. Rey, Mechanisms of action and therapeutic potential of strontium in bone, Calcif. Tissue Int. 69 (2001) 121–129, https://doi.org/10.1007/s002230010055.
[29] E. Bonnelye, A. Chabadel, F. Saltel, P. Jurdic, Dual effect of strontium ranelate: stimulation of osteoblast differentiation and inhibition of osteoclast formation and resorption in vitro, Bone 42 (2008) 129–138, https://doi.org/10.1016/j.bone.2007.08.043.
[30] S. Tadier, R. Bareille, R. Siadous, O. Marsan, C. Charvillat, S. Cazalbou, J. Amédée, C. Rey, C. Combes, Strontium-loaded mineral bone cements as sustained release systems: compositions, release properties, and effects on human osteoprogenitor cells, J. Biomed. Mater. Res. B 100B (2012) 378–390, https://doi.org/10.1002/jbm.b.31959.
[31] U. Thormann, S. Ray, U. Sommer, T. ElKhassawna, T. Rehling, M. Hundgeburth, A. Henß, M. Rohnke, J. Janek, K.S. Lips, C. Heiss, G. Schlewitz, G. Szalay, M. Schumacher, M. Gelinsky, R. Schnettler, V. Alt, Bone formation induced by strontium modified calcium phosphate cement in critical-size metaphyseal fracture defects in ovariectomized rats, Biomaterials 34 (2013) 8589–8598, https://doi.org/10.1016/j.biomaterials.2013.07.036.
[32] F. Salamanna, G. Giavaresi, D. Contartese, A. Bigi, E. Boanini, A. Parrilli, R. Lolli, A. Gasbarrini, G. Barbanti Brodano, M. Fini, Effect of strontium substituted ß-TCP associated to mesenchymal stem cells from bone marrow and adipose tissue on spinal fusion in healthy and ovariectomized rat, J. Cell. Physiol. 234 (2019) 20046–20056, https://doi.org/10.1002/jcp.28601.
[33] F. Salamanna, G. Giavaresi, A. Parrilli, P. Torricelli, E. Boanini, A. Bigi, M. Fini, Antiresorptive properties of strontium substituted and alendronate functionalized hydroxyapatite nanocrystals in an ovariectomized rat spinal arthrodesis model, Mater. Sci. Eng. C Mater. Biol. Appl. 95 (2019) 355–362, https://doi.org/10.1016/j.msec.2017.11.016.
[34] M. Schumacher, A.S. Wagner, J. Kokesch-Himmelreich, A. Bernhardt, M. Rohnke, S. Wenisch, M. Gelinsky, Strontium substitution in apatitic CaP cements effectively

attenuates osteoclastic resorption but does not inhibit osteoclastogenesis, Acta Biomater. 37 (2016) 184–194, https://doi.org/10.1016/j.actbio.2016.04.016.
[35] S. Sprio, M. Dapporto, M. Montesi, S. Panseri, W. Lattanzi, E. Pola, G. Logroscino, A. Tampieri, Novel osteointegrative sr-substituted apatitic cements enriched with alginate, Materials 9 (2016) 763, https://doi.org/10.3390/ma9090763.
[36] M. Montesi, S. Panseri, M. Dapporto, A. Tampieri, S. Sprio, Sr-substituted bone cements direct mesenchymal stem cells, osteoblasts and osteoclasts fate, PLoS One 12 (2017) e0172100, https://doi.org/10.1371/journal.pone.0172100.
[37] E. Boanini, S. Pagani, M. Tschon, K. Rubini, M. Fini, A. Bigi, Monetite vs. brushite: different influences on bone cell response modulated by strontium functionalization, J. Funct. Biomater. 13 (2022) 65, https://doi.org/10.3390/jfb13020065.
[38] S.J. Gallacher, T. Dixon, Impact of treatments for postmenopausal osteoporosis (bisphosphonates, parathyroid hormone, strontium ranelate and denosumab) on bone quality: a systematic review, Calcif. Tissue Int. 87 (2010) 469–484, https://doi.org/10.1007/s00223-010-9420-x.
[39] B. Kołodziejska, N. Stępień, J. Kolmas, The influence of strontium on bone tissue metabolism and its application in osteoporosis treatment, Int. J. Mol. Sci. 22 (2021) 6564, https://doi.org/10.3390/ijms22126564.
[40] S. Vahabzadeh, S. Fleck, M. Krishna Duvvuru, H. Cummings, Effects of cobalt on physical and mechanical properties and in vitro degradation behavior of brushite cement, JOM 71 (2019) 315–320, https://doi.org/10.1007/s11837-018-3204-6.
[41] J.V. Rau, I.V. Fadeeva, A.A. Forysenkova, G.A. Davydova, M. Fosca, Y.Y. Filippov, I.V. Antoniac, A. Antoniac, A. D'Arco, M. Di Fabrizio, M. Petrarca, S. Lupi, M. Di Menno, V.G. Di Bucchianico, V.I. Yankova, M.B. Cristea Putlayev, Strontium substituted tricalcium phosphate bone cement: short and long-term time-resolved studies and in vitro properties, Adv. Mater. Interfaces 9 (2022) 2200803, https://doi.org/10.1002/admi.202200803.
[42] J. Dai, Y. Fu, D. Chen, Z. Sun, A novel and injectable strontium-containing hydroxyapatite bone cement for bone substitution: a systematic evaluation, Mater. Sci. Eng. C Mater. Biol. Appl. 124 (2021) 112052, https://doi.org/10.1016/j.msec.2021.112052.
[43] T. Wu, S. Yang, T. Lu, F. He, J. Zhang, H. Shi, Z. Lin, J. Ye, Strontium ranelate simultaneously improves the radiopacity and osteogenesis of calcium phosphate cement, Biomed. Mater. 14 (2019) 035005, https://doi.org/10.1088/1748-605X/ab052d.
[44] E. Boanini, F. Silingardi, M. Gazzano, A. Bigi, Synthesis and hydrolysis of brushite (DCPD): the role of ionic substitution, Cryst. Growth Des. 21 (2021) 1689–1697, https://doi.org/10.1021/acs.cgd.0c01569.
[45] W.E. Brown, L.C. Chow, Dental resptorative cement pastes, US Pat. 4518430 (1985) (May, 21).
[46] T.D. Schmittgen, K.J. Livak, Analyzing real-time PCR data by the comparative C(T) method, Nat. Protoc. 3 (2008) 1101–1108, https://doi.org/10.1038/nprot.2008.73.
[47] T. Yu, S. Zeng, X. Liu, H. Shi, J. Ye, C. Zhou, Application of Sr-doped octacalcium phosphate as a novel Sr carrier in the α-tricalcium phosphate bone cement, Ceram. Int. 43 (2017) 12579–12587, https://doi.org/10.1016/j.ceramint.2017.06.135.
[48] H.B. Pan, Z.Y. Li, W.M. Lam, J.C. Wong, B.W. Darvell, K.D.K. Luk, W.W. Lu, Solubility of strontium-substituted apatite by solid titration, Acta Biomater. 5 (2009) 1678–1685, https://doi.org/10.1016/j.actbio.2008.11.032.
[49] A.B. Celil, J.O. Hollinger, P.G. Campbell, Osx transcriptional regulation is mediated by additional pathways to BMP2/Smad signaling, J. Cell. Biochem. 95 (2005) 518–528, https://doi.org/10.1002/jcb.20429.
[50] Q. Liu, M. Li, S. Wang, Z. Xiao, Y. Xiong, G. Wang, Recent advances of osterix transcription factor in osteoblast differentiation and bone formation, Front. Cell Dev. Biol. 8 (2020) 601224, https://doi.org/10.3389/fcell.2020.601224.
[51] X. Qin, Q. Jiang, H. Komori, C. Sakane, R. Fukuyama, Y. Matsuo, K. Ito, T. Miyazaki, T. Komori, Runt-related transcription factor-2 (Runx2) is required for bone matrix protein gene expression in committed osteoblasts in mice, J. Bone Miner. Res. 36 (2021) 2081–2095, https://doi.org/10.1002/jbmr.4386.
[52] M.J. Ortuño, A.R. Susperregui, N. Artigas, J.L. Rosa, F. Ventura, Osterix induces Col1a1 gene expression through binding to Sp1 sites in the bone enhancer and proximal promoter regions, Bone 52 (2013) 548–556, https://doi.org/10.1016/j.bone.2012.11.007.
[53] J.H. Jonason, G. Xiao, M. Zhang, L. Xing, D. Chen, Post-translational regulation of Runx2 in bone and cartilage, J. Dent. Res. 88 (2009) 693–703, https://doi.org/10.1177/0022034509341629.
[54] S. Kannan, J. Ghosh, S.K. Dhara, Osteogenic differentiation potential of porcine bone marrow mesenchymal stem cell subpopulations selected in different basal media, Biol. Open 9 (2020) bio053280, https://doi.org/10.1242/bio.053280.
[55] J.M. Kim, C. Lin, Z. Stavre, M.B. Greenblatt, J.H. Shim, Osteoblast-osteoclast communication and bone homeostasis, Cells 9 (2020) 2073, https://doi.org/10.3390/cells9092073.
[56] S. Bolamperti, I. Villa, A. Rubinacci, Bone remodeling: an operational process ensuring survival and bone mechanical competence, Bone Res. 10 (2022) 48, https://doi.org/10.1038/s41413-022-00219-8.
[57] H. Winet, The role of microvasculature in normal and perturbed bone healing as revealed by intravital microscopy, Bone 19 (1996) 39S–57S, https://doi.org/10.1016/S8756-3282(96)00133-0.